

REPORT DOCUMENTATION PAGE

Form Approved
OMB No. 0704-0188

Public reporting burden for this collection of information is estimated to average 1 hour per response, including the time for reviewing instructions, searching existing data sources, gathering and maintaining the data needed, and completing and reviewing this collection of information. Send comments regarding this burden estimate or any other aspect of this collection of information, including suggestions for reducing this burden to Department of Defense, Washington Headquarters Services, Directorate for Information Operations and Reports (0704-0188), 1215 Jefferson Davis Highway, Suite 1204, Arlington, VA 22202-4302. Respondents should be aware that notwithstanding any other provision of law, no person shall be subject to any penalty for failing to comply with a collection of information if it does not display a currently valid OMB control number. **PLEASE DO NOT RETURN YOUR FORM TO THE ABOVE ADDRESS.**

1. REPORT DATE (DD-MM-YYYY) January 2015	2. REPORT TYPE Technical Paper	3. DATES COVERED (From - To) January 2015-March 2015	
4. TITLE AND SUBTITLE Non-Equilibrium Modeling of Inductively Coupled RF Plasmas		5a. CONTRACT NUMBER In-House	
		5b. GRANT NUMBER	
		5c. PROGRAM ELEMENT NUMBER	
6. AUTHOR(S) A. Munafo, J-L. Cambier, and M. Panesi		5d. PROJECT NUMBER	
		5e. TASK NUMBER	
		5f. WORK UNIT NUMBER Q1AM	
7. PERFORMING ORGANIZATION NAME(S) AND ADDRESS(ES) Air Force Research Laboratory (AFMC) AFRL/RQRS 1 Ara Drive. Edwards AFB, CA 93524-7013		8. PERFORMING ORGANIZATION REPORT NO.	
9. SPONSORING / MONITORING AGENCY NAME(S) AND ADDRESS(ES) Air Force Research Laboratory (AFMC) AFRL/RQR 5 Pollux Drive Edwards AFB CA 93524-7048		10. SPONSOR/MONITOR'S ACRONYM(S)	
		11. SPONSOR/MONITOR'S REPORT NUMBER(S) AFRL-RQ-ED-TP-2015-064	
12. DISTRIBUTION / AVAILABILITY STATEMENT Distribution A: Approved for Public Release; Distribution Unlimited.			
13. SUPPLEMENTARY NOTES Technical paper presented at 8th European Symposium on Aerothermodynamics for Space Vehicles, Lisbon, Portugal; 2-6 Mar 2015. PA#15120			
14. ABSTRACT This paper discusses the modeling of non-equilibrium effects in inductively coupled plasma facilities. The model relies on the solution of the Navier-Stokes and Maxwell equations in a one-dimensional geometry. Steady-state solutions are obtained by means of an implicit Finite Volume method. Non-equilibrium effects are treated by means of a hybrid State-to-State formulation. The electronic states of atoms are treated as separate species, allowing for non-Boltzmann distributions of their populations. Thermal non-equilibrium between the translation and vibrational of heavy-particles is accounted for by means of a multi-temperature approach. The results show that non-equilibrium plays an important role close to the walls, due to the combined effects of Ohming heating, and chemical composition and temperature gradients.			
15. SUBJECT TERMS			
16. SECURITY CLASSIFICATION OF: a. REPORT Unclassified		17. LIMITATION OF ABSTRACT SAR	18. NUMBER OF PAGES 12
b. ABSTRACT Unclassified		19a. NAME OF RESPONSIBLE PERSON Jean-Luc Cambier	
c. THIS PAGE Unclassified		19b. TELEPHONE NO (include area code) 661-525-5649	

Standard Form
298 (Rev. 8-98)
Prescribed by ANSI
Std. 239.18

NON-EQUILIBRIUM MODELING OF INDUCTIVELY COUPLED RF PLASMAS

Alessandro Munafò¹, Jean-Luc Cambier², and Marco Panesi³

¹*University of Illinois at Urbana-Champaign, Talbot Laboratory, 104 S. Wright St., Urbana, IL 61801, USA*

²*Edwards Air Force Base Research Laboratory, 10 E. Saturn Blvd., CA 93524, USA*

³*University of Illinois at Urbana-Champaign, Talbot Laboratory, 104 S. Wright St., Urbana, IL 61801, USA*

ABSTRACT

This paper discusses the modeling of non-equilibrium effects in inductively coupled plasma facilities. The model relies on the solution of the Navier-Stokes and Maxwell equations in a one-dimensional geometry. Steady-state solutions are obtained by means of an implicit Finite Volume method. Non-equilibrium effects are treated by means of a hybrid State-to-State formulation. The electronic states of atoms are treated as separate species, allowing for non-Boltzmann distributions of their populations. Thermal non-equilibrium between the translation and vibrational of heavy-particles is accounted for by means of a multi-temperature approach. The results show that non-equilibrium plays an important role close to the walls, due to the combined effects of Ohming heating, and chemical composition and temperature gradients.

Key words: NLTE plasmas, State-to-State modeling, Inductively Coupled Plasma torch.

1. INTRODUCTION

Inductively coupled plasma (ICP) torches have wide range of possible applications which include deposition of metal coatings, synthesis of ultra-fine powders, generation of high purity silicon and testing of thermal protection materials for atmospheric entry vehicles [1, 2].

In its simplest configuration, an ICP torch consists of a quartz tube surrounded by an inductor coil made of a series of parallel current-carrying rings. The radio-frequency (RF) currents running through the inductor induce toroidal currents in the gas which is heated thanks to Ohmic dissipation [2, 3]. If the energy supplied is large enough, the gas flowing through the torch can undergo ionization, leading to the formation of a plasma.

The accurate modeling of the flow-field and electromagnetic phenomena inside an ICP torch requires the coupled solution of the Navier-Stokes and Maxwell equations [2]. In literature, the Local Thermodynamic Equilibrium (LTE) assumption is often used to describe the state of the gas in the discharge region [4–17]. However,

Non Local Thermodynamic Equilibrium (NLTE) simulations of Argon [18, 19] and air plasmas [20], have shown that the LTE assumption may not always hold.

An accurate modeling of NLTE effects in ICP RF plasmas can be achieved by means of State-to-State models [21–33]. These treat each internal energy state as a separate *pseudo species*, thus allowing for non-Boltzmann distributions. Rate coefficients are usually obtained through quantum chemistry calculations [34–39] or through phenomenological models [40, 41]. State-to-State models provide a superior description compared to conventional multi-temperature models, which are based on Maxwell-Boltzmann distributions [42–45]. However, due to the large number of governing equations to be solved, their application to multi-dimensional problems can become computationally demanding [46–50].

The purpose of the present work is the development of a magneto-hydrodynamic NLTE model for an ICP torch. The flow model has to be simple enough to allow for the implementation of sophisticated NLTE models describing the kinetics of atoms and molecules in the inductor region. The final goal is the assessment of the extent of non-equilibrium phenomena occurring in ICP generators used for Thermal Protection System (TPS) testing.

The paper is structured as follows. Section 2 describes the physical model. The numerical method is presented in Sect. 3. Computational results are discussed in Sect. 4. Conclusions are outlined in Sect. 5.

2. PHYSICAL MODELING

The NLTE model for the ICP torch is built based on the torch geometry displayed in Figure 1. To make the problem tractable, the following assumptions are introduced:

- (i) Constant pressure and no *macroscopic streaming*,
- (ii) Charge neutrality and no displacement current,
- (iii) Steady-state conditions for gas quantities (i.e., $\partial(\cdot)/\partial t = 0$),
- (iv) No gradients along the axial and circumferential directions (i.e., $\partial(\cdot)/\partial z = 0$, $\partial(\cdot)/\partial \phi = 0$).

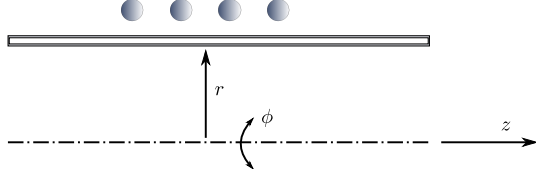


Figure 1: Torch geometry and adopted reference frame.

2.1. Electromagnetic field

The electromagnetic field inside the ICP torch is described by the Maxwell equations:

$$\nabla \cdot \mathbf{E} = \frac{\rho^c}{\epsilon_0} \quad (1)$$

$$\nabla \cdot \mathbf{B} = 0 \quad (2)$$

$$\nabla \times \mathbf{E} = -\frac{\partial \mathbf{B}}{\partial t} \quad (3)$$

$$\nabla \times \mathbf{B} = \mu_0 \mathbf{J} + \mu_0 \epsilon_0 \frac{\partial \mathbf{E}}{\partial t} \quad (4)$$

where quantities \mathbf{E} and \mathbf{B} are the electric and magnetic fields, respectively. Quantity ρ^c stands for the charge density. The current density \mathbf{J} is assumed to obey Ohm's law $\mathbf{J} = \sigma_e \mathbf{E}$ [51], with σ_e being the electrical conductivity. Quantities ϵ_0 and μ_0 are the vacuum permittivity and magnetic permeability, respectively. The application of the simplifying assumptions just introduced to the Maxwell equations (1)-(4) leads to the following induction equation for the induced toroidal electric field:

$$\frac{\partial}{\partial r} \left(\frac{1}{r} \frac{\partial r E_\phi}{\partial r} \right) = -\mu_0 \sigma_e \frac{\partial E_\phi}{\partial t} \quad (5)$$

Since the induced eddy currents which are responsible for the heating of the gas are induced by a primary current whose intensity varies sinusoidally in time, it seems natural to seek for a mono-chromatic wave solution, $E_\phi = E \exp(i2\pi ft)$, where f is the frequency of the primary current. To account for the possible phase difference between the induced electric and magnetic fields, the amplitude E is taken complex, $E = E_{\text{re}} + iE_{\text{im}}$. The substitution of $E \exp(i2\pi ft)$ in Eq. (5) leads to:

$$0 \times \frac{\partial r \mathbf{U}_{\text{em}}}{\partial t} + \frac{\partial r \mathbf{F}_{\text{em}}}{\partial r} = r \mathbf{S}_{\text{em}} \quad (6)$$

The electromagnetic (em) conservative variable, flux and source term vectors are:

$$\mathbf{U}_{\text{em}} = [E_{\text{re}} \quad E_{\text{im}}]^T \quad (7)$$

$$\mathbf{F}_{\text{em}} = \left[\frac{\partial E_{\text{re}}}{\partial r} \quad \frac{\partial E_{\text{im}}}{\partial r} \right]^T \quad (8)$$

$$\mathbf{S}_{\text{em}} = \left[\frac{E_{\text{re}}}{r^2} + \omega \mu_0 \sigma_e E_{\text{im}} \quad \frac{E_{\text{im}}}{r^2} - \omega \mu_0 \sigma_e E_{\text{re}} \right]^T \quad (9)$$

where the angular frequency is $\omega = 2\pi f$. The symbol T denotes the transpose operator.

Equation (6) must be supplemented with boundary conditions at the axis ($r = 0$) and at the torch wall ($r = R$, with R being the torch radius). On the axis, due to symmetry, both the real and imaginary components of the induced electric field must vanish:

$$E_{\text{re}} = 0, \quad E_{\text{im}} = 0, \quad \text{at } r = 0 \quad (10)$$

The boundary condition at the torch wall is obtained as follows. The amplitudes of the toroidal electric field and the axial magnetic field are linked via [17]:

$$\frac{1}{r} \frac{\partial r E}{\partial r} = -\omega B \quad (11)$$

where the amplitude B is taken complex. Immediately outside the wall the magnetic field must be real and, since there is no plasma outside the tube, its value can only depend on the ICP operating conditions and characteristics. If the torch is long enough, the magnetic field at the torch wall can be approximated with the expression for an infinite solenoid, $B(r = R) = \mu_0 N I_c$, where quantities N and I_c are the number of turns per unit-length and the amplitude of the primary current. The evaluation of Eq. (11) at the torch wall and the use of the relation $B(r = R) = \mu_0 N I_c$ gives the wall boundary condition for the induced electric field:

$$\frac{1}{r} \frac{\partial r E_{\text{re}}}{\partial r} = 0, \quad \frac{1}{r} \frac{\partial r E_{\text{im}}}{\partial r} = -\omega \mu_0 N I_c, \quad \text{at } r = R \quad (12)$$

2.2. Gas field

The gas contained in the torch is made of electrons, atoms and (diatomic) molecules. Charged particles comprise electrons and positively singly charged ions. The set \mathcal{S} stores the chemical components, and the heavy-particles are stored in the set \mathcal{S}_h . The atomic and molecular components are stored in the sets \mathcal{S}_a and \mathcal{S}_m , respectively. The previously introduced sets satisfy the relations $\mathcal{S}_h = \mathcal{S}_a \cup \mathcal{S}_m$ and $\mathcal{S} = \{e^-\} \cup \mathcal{S}_m$, where the symbol e^- indicates the free-electrons. The electronic levels of the heavy components are stored in sets $\mathcal{I}_s^{\text{el}}$ (with $s \in \mathcal{S}_h$) and are treated as separate *pseudo-species* based on a State-to-State approach [52]. The notation s_i is then introduced to denote the i -th electronic level of the heavy component $s \in \mathcal{S}_h$, with the related degeneracy and energy being $g_{s_i}^{\text{el}}$ and $E_{s_i}^{\text{el}}$, respectively. A multi-temperature model is instead used for vibration of molecules and translation of free-electrons (with the related temperatures being T_v and T_e , respectively) [53]. Rotational non-equilibrium effects are disregarded.

Thermodynamics

The gas pressure is computed based on Dalton's law of partial pressures by summing the contributions of free-electrons and heavy-particles, $p = p_e + p_h$, where the

symbol k_B stands for Boltzmann's constant. The partial pressures of free-electrons and heavy-particles are, respectively, $p_e = n_e k_B T^e$ and $p_h = n_h k_B T$, where quantities n_e and n_h denote, respectively, the related the number densities. The number density of heavy-particles is obtained via $n_h = \sum_{s \in \mathcal{S}_h} n_s$, with $n_s = \sum_{i \in \mathcal{I}_s^{\text{el}}} n_{s_i}$.

The gas total, vibrational and free-electron energy densities read:

$$\rho e = \frac{3}{2}p + \sum_{s \in \mathcal{S}_m} n_s [\tilde{E}_s^r(T) + \tilde{E}_s^v(T_v)] + \sum_{s \in \mathcal{S}_h} n_s \Delta E_s^f + \sum_{\substack{s \in \mathcal{S}_h \\ i \in \mathcal{I}_s^{\text{el}}}} n_{s_i} E_{s_i}^{\text{el}} \quad (13)$$

$$\rho e_v = \sum_{s \in \mathcal{S}_m} n_s \tilde{E}_s^v(T_v), \quad \rho e_e = \frac{3}{2}p_e \quad (14)$$

Quantity ΔE_s^f stands for the formation energy (per particle) of the heavy component $s \in \mathcal{S}_h$. The average particle rotational and vibrational energies (\tilde{E}_s^r and \tilde{E}_s^v , $s \in \mathcal{S}_m$, respectively) are computed, respectively, according to the rigid-rotor and harmonic-oscillator models [54].

Thermodynamic data used in this work are taken from Gurvich tables [55] (with the exception of the spectroscopic data for the electronic levels taken from [26]).

Kinetics

Collisional processes The NLTE model for ICP RF plasmas developed in this work accounts for the following kinetic processes:

- (i) Excitation by electron impact (EX_e),
- (ii) Ionization by electron impact (I_e),
- (iii) Dissociation by electron impact (D_e),
- (iv) Dissociation by heavy-particle impact (D_h),
- (v) Associative ionization (AI).

Rate coefficients and production terms The endothermic rate coefficients for electron induced processes and associative ionization reactions are taken from the ABBA model [26–29]. Those for dissociation by heavy-particle impact are taken from the work of Park [43]. Reverse rate coefficients are obtained based on micro-reversibility [56, 57].

The mass production terms for free-electrons and heavy-particles due to the kinetic processes considered in this work are computed based on the zeroth-order reaction rate theory [56, 57]. In what follows, the latter quantities are indicated with the notation ω_e and ω_{s_i} .

The energy transfer terms for the gas vibrational energy account for (i) vibrational-translational (vt) energy exchange in molecule heavy-particle collisions, (ii) vibrational-electron (ve) energy exchange in molecule electron collisions, and (iii) the creation/destruction of vibrational energy in chemical reactions (cv). The first two energy transfer terms (indicated in what follows with Ω_{vt} and Ω_{ve} , respectively) are evaluated based on a Landau-Teller model [58], while the chemistry-vibration coupling term (Ω_{cv}) is computed by using the non-preferential dissociation model of Candler [59]. The relaxation times for vt energy transfer are computed by means of the modified formula of Millikan and White proposed by Park [43]. The energy transfer in molecule-electron inelastic collisions is considered only for N_2 . The corresponding relaxation time is taken from the work of Bourdon [60].

The energy transfer terms for the free-electron gas account for energy exchange undergone by free-electrons in (i) elastic collisions with heavy-particles (Ω_{el}), (ii) inelastic electron induced excitation, ionization and dissociation processes (Ω_{in}) and (iii) Joule heating (Ω_j). The expressions for the first two can be found in [27–29]. The (time-averaged) Joule heating source term is obtained by averaging over a period the instantaneous Joule heating power and reads [15, 17]:

$$\Omega_j = \frac{1}{2} \sigma_e (E_{\text{re}}^2 + E_{\text{im}}^2) \quad (15)$$

Transport

Transport phenomena are treated based on the results obtained from the application of the Chapman-Enskog method to the Boltzmann equation [61]. In the present work, transport phenomena are modeled by assuming that (i) inelastic and reactive collisions have a no effect on the transport properties and fluxes and (ii) the collision cross-sections for elastic scattering do not depend on the internal quantum states. In view of the last assumption, the dimension of the transport matrices shrinks from the number of species to the number of chemical components.

Heavy-particle gas The translational component of thermal conductivity (λ_t) is:

$$\lambda_t = \sum_{s \in \mathcal{S}_h} \alpha_s^\lambda X_s \quad (16)$$

where the mole fractions of the heavy components are $X_s = n_s k_B T / p$ ($s \in \mathcal{S}_h$). The coefficients α_s^λ are solution of the linear (symmetric) transport system:

$$\sum_{p \in \mathcal{S}_h} G_{sp}^\lambda \alpha_s^\lambda = X_s \quad (17)$$

$s \in \mathcal{S}_h$. Quantities G_{sp}^λ are the entries of the thermal conductivity (symmetric) transport matrix [56]. The contributions of the gas rotational and vibrational degrees of

freedom to the thermal conductivity (λ_r and λ_v , respectively) are taken into account by means of the generalized Eucken's correction [56].

Electron gas The thermal and electrical conductivity of the electron gas are (in the second and third-order Laguerre-Sonine approximations, respectively) [62, 63]:

$$\lambda_e = \frac{75}{8} k_B \sqrt{\frac{2\pi k_B T_e}{m_e}} \frac{X_e \Lambda_{ee}^{22}}{\Lambda_{ee}^{11} \Lambda_{ee}^{22} - (\Lambda_{ee}^{12})^2} \quad (18)$$

$$\sigma_e = \frac{3}{2} \frac{e^2}{k_B} \sqrt{\frac{2\pi k_B}{m_e T_e}} \frac{X_e \Lambda_{ee}^{11}}{\Lambda_{ee}^{00} \Lambda_{ee}^{11} - (\Lambda_{ee}^{10})^2} \quad (19)$$

where the mole fraction of free-electrons is $X_e = n_e k_B T_e / p$ and $e = 1.602 \times 10^{-19} \text{ C}$ is the electron charge. Quantities $\Lambda_{ee}^{i,j}$ are the Devoto collision integrals [62].

Mass diffusion and heat fluxes The mass diffusion fluxes are found by solving the Stefan-Maxwell equations under the constraints of global mass conservation and ambipolar diffusion [62–65]. The diffusion driving forces include only mole fraction gradients (thermal and baro diffusion are both neglected). In view of the assumed independence of the elastic collision cross-section on the internal quantum states, the Stefan-Maxwell equations are solved for the free-electron and heavy component diffusion fluxes (J_e and J_s , $s \in \mathcal{S}_h$, respectively). The mass diffusion fluxes for the internal (electronic) levels are then found as shown in [17]. The total, vibrational and free-electron heat fluxes are:

$$q = \sum_{s \in \mathcal{S}_h} \left(\frac{5}{2} k_B T + \Delta E_s^f \right) \frac{J_s}{m_s} + \sum_{s \in \mathcal{S}_m} \tilde{E}_s^r(T) \frac{J_s}{m_s} + \sum_{\substack{s \in \mathcal{S}_h \\ i \in \mathcal{I}_s^{\text{el}}}} E_{s_i}^{\text{el}} \frac{J_{s_i}}{m_s} - \lambda_{\text{tr}} \frac{\partial T}{\partial r} + q_v + q_e \quad (20)$$

$$q_v = \sum_{s \in \mathcal{S}_m} \tilde{E}_s^v(T_v) \frac{J_s}{m_s} - \lambda_v \frac{\partial T_v}{\partial r} \quad (21)$$

$$q_e = \left(\frac{5}{2} k_B T_e \right) \frac{J_e}{m_e} - \lambda_e \frac{\partial T_e}{\partial r} \quad (22)$$

where the translational-rotational thermal conductivity of the heavy-particle gas is $\lambda_{\text{tr}} = \lambda_t + \lambda_r$.

Governing equations

The governing equations for the gas chemical composition and temperature distribution in the ICP torch are:

$$\frac{\partial r \mathbf{U}_g}{\partial t} + \frac{\partial r \mathbf{F}_g}{\partial r} = r \mathbf{S}_g \quad (23)$$

where the gas (g) conservative variable, flux and source term vectors are:

$$\mathbf{U}_g = [\rho_e \quad \rho_{s_i} \quad \rho_e \quad \rho e_v \quad \rho e_e]^T \quad (24)$$

$$\mathbf{F}_g = [J_e \quad J_{s_i} \quad q \quad q_v \quad q_e]^T \quad (25)$$

$$\mathbf{S}_g = [\omega_e \quad \omega_{s_i} \quad \Omega_j \quad \Omega_v \quad \Omega_e]^T \quad (26)$$

$i \in \mathcal{I}_s^{\text{el}}$, $s \in \mathcal{S}_h$, with $\Omega_v = \Omega_{vt} + \Omega_{ve} + \Omega_{cv}$ and $\Omega_e = \Omega_{el} + \Omega_{in} + \Omega_j$.

The boundary conditions used for solving Eq. (23) are a symmetry boundary condition at the axis and an isothermal non-catalytic boundary condition at the torch wall (with the related imposed wall temperature indicated with T_w). In analogy with the work of Mostaghimi *et al.* [18, 19], an adiabatic boundary condition is used for the vibrational and free-electron temperatures at the torch wall.

3. NUMERICAL METHOD

3.1. Coupled formulation

The governing equations for the gas and the electromagnetic fields are strongly coupled due to the presence of the Joule heating term in Eq. (26) and the electrical conductivity in Eq. (9). This suggests to adopt a fully coupled approach by casting Eqs. (6) and (23):

$$\frac{\partial r \mathbf{\Gamma} \mathbf{U}}{\partial t} + \frac{\partial r \mathbf{F}}{\partial r} = \mathbf{S} \quad (27)$$

where conservative variable, flux and source term vectors are now $\mathbf{U} = (\mathbf{U}_g, \mathbf{U}_{\text{em}})$, $\mathbf{F} = (\mathbf{F}_g, \mathbf{F}_{\text{em}})$ and $\mathbf{S} = (\mathbf{S}_g, \mathbf{S}_{\text{em}})$. The matrix $\mathbf{\Gamma}$ in Eq. (27) reads:

$$\mathbf{\Gamma} = \begin{pmatrix} 1 & 0 & 0 & 0 & 0 & 0 & 0 \\ 0 & \delta_{s_i p_j} & 0 & 0 & 0 & 0 & 0 \\ 0 & 0 & 1 & 0 & 0 & 0 & 0 \\ 0 & 0 & 0 & 1 & 0 & 0 & 0 \\ 0 & 0 & 0 & 0 & 1 & 0 & 0 \\ 0 & 0 & 0 & 0 & 0 & 0 & 0 \\ 0 & 0 & 0 & 0 & 0 & 0 & 0 \end{pmatrix} \quad (28)$$

$i \in \mathcal{I}_s^{\text{el}}$, $j \in \mathcal{I}_p^{\text{el}}$, $s, p \in \mathcal{S}_h$, where $\delta_{s_i p_j} = \delta_{sp} \delta_{ij}$, with δ being Kronecker's delta.

3.2. Spatial discretization

The application of the Finite Volume method to Eq. (27) leads to the following ODE describing the time-evolution of the conservative variables of cell c :

$$\mathbf{\Gamma} \frac{\partial \mathbf{U}_c}{\partial t} r_c \Delta r_c + r_{c+\frac{1}{2}} \mathbf{F}_{c+\frac{1}{2}} - r_{c-\frac{1}{2}} \mathbf{F}_{c-\frac{1}{2}} = \mathbf{S}_c r_c \Delta r_c \quad (29)$$

with the cell volume (length) and centroid location being $\Delta r_c = r_{c+1/2} - r_{c-1/2}$ and $r_c = 1/2(r_{c+1/2} +$

$r_{c-1/2}$), respectively. The evaluation of the diffusive flux $\mathbf{F}_{c+1/2}$ is performed by approximating the values and the gradients of a given quantity p (e.g., temperatures and electric field components) by means of an arithmetic average and a second order central finite difference, respectively. To facilitate the implementation of the constant pressure constraint, the solution update is performed on primitive variables consisting of mass fractions, temperatures and electric field components, $\mathbf{P} = (y_e, y_{s_i}, T, T_v, T_e, E_{re}, E_{im})$:

$$\Gamma \mathbf{T}_c \frac{\partial \mathbf{P}_c}{\partial t} r_c \Delta r_c + r_{c+\frac{1}{2}} \mathbf{F}_{c+\frac{1}{2}} - r_{c-\frac{1}{2}} \mathbf{F}_{c-\frac{1}{2}} = \mathbf{S}_c r_c \Delta r_c \quad (30)$$

The transformation matrix \mathbf{T} can be easily obtained from the time-derivative of the conservative variables $(\partial \mathbf{U} / \partial t)$ by exploiting the global continuity equation (i.e., $\partial \rho / \partial t = 0$).

3.3. Temporal discretization

Equation (30) is integrated in time by means of the backward Euler method [66]:

$$\Gamma \mathbf{T}_c^n \frac{\delta \mathbf{P}_c^n}{\Delta t_c} r_c \Delta r_c + r_{c+\frac{1}{2}} \mathbf{F}_{c+\frac{1}{2}}^{n+1} - r_{c-\frac{1}{2}} \mathbf{F}_{c-\frac{1}{2}}^{n+1} = \mathbf{S}_c^{n+1} r_c \Delta r_c \quad (31)$$

where $\delta \mathbf{P}_c^n = \mathbf{P}_c^{n+1} - \mathbf{P}_c^n$. The local time-step Δt is computed based on the von Neumann number (ξ) as $\Delta t = \xi / (2\rho^d)$ [67], where quantity ρ^d stands for the spectral radius of the diffusive flux Jacobian $\partial \mathbf{F} / \partial \mathbf{U}$.

In order to advance the solution from the time-level n to the time-level $n + 1$, Eq. (31) is linearized around the time-level n . To facilitate the linearization procedure, the flux \mathbf{F} is written as $\mathbf{F} = \mathbf{A} \partial \mathbf{P} / \partial r$ and the matrix \mathbf{A} is kept frozen during the linearization. The source term is linearized by evaluating the related Jacobian analytically to enhance stability. The outcome of the linearization procedure is a block-tridiagonal algebraic system to be solved at each time-step:

$$\mathbf{M}_L^n \delta \mathbf{P}_{c-1}^n + \mathbf{M}_C^n \delta \mathbf{P}_c^n + \mathbf{M}_R^n \delta \mathbf{P}_{c+1}^n = -\mathbf{R}_c^n \quad (32)$$

where the right-hand-side residual is:

$$\mathbf{R}_i = - \left(r_{c+\frac{1}{2}} \mathbf{F}_{c+\frac{1}{2}} - r_{c-\frac{1}{2}} \mathbf{F}_{c-\frac{1}{2}} \right) + \mathbf{S}_c r_c \Delta r_c \quad (33)$$

The left (L), central (C) and right (R) block matrices can be found from the linearization procedure (see, for instance, [68] for more details). The block-tridiagonal system (32) is solved by means of Thomas' algorithm [67] and the solution updated at the time-level $n + 1$, $\mathbf{P}_c^{n+1} = \mathbf{P}_c^n + \delta \mathbf{P}_c^n$. This process is continued until steady-state is reached.

Boundary conditions are implemented through ghost cells [67] and the related folding in the central block matrices \mathbf{M}_C is performed as suggested by Candler [59].

4. COMPUTATIONAL RESULTS

The gas contained in torch consists of nitrogen molecules and the related dissociation and ionization products (i.e., $\mathcal{S} = \{e, N, N_2, N_2^+, N^+\}$). Simulations are performed by means of the ABBA State-to-State (StS) model [26–29] and the multi-temperature (MT) model proposed by Park [43].

The torch radius, the number of coils per unit-length, the frequency of the primary current and the wall temperature are set to 0.08 m, 50, 0.5 MHz and 350 K, respectively. The current intensity of the primary circuit is not prescribed. Instead the former is found from the solution by imposing that the dissipated power (per unit-length) in the plasma:

$$P = 2\pi \int_0^R \Omega_j r dr, \quad (34)$$

is equal to $P_0 = 350\,000$ W/m. In order to match the condition $P = P_0$ at steady-state, the current intensity is multiplied by the scaling factor $\gamma = \sqrt{P_0 / P}$ after updating the solution at each time-step [12, 16]. Three different values are adopted for the pressure in the torch: 3000 Pa, 5000 Pa and 10 000 Pa.

In all the cases, the solution is initialized with a uniform equilibrium distribution at 7500 K (with both electric field components equal to 0.1 V/m). The starting of the simulation is quite violent. Severe temperature and chemical composition gradients occur at the wall, due to the cold temperature imposed. During this initial phase (in particular when using the StS model), the time-step must be limited to avoid numerical instabilities. For this reason, during the first few iterations, the von Neumann number is kept within the range 1000–10 000. Once the initial transient passed, its value is increased interactively (up to 500 000 000) to accelerate convergence to steady-state. Such large values are possible due to the adoption of a fully coupled implicit time-integration method.

For the conditions adopted in the present work, the vibrational and free-electron temperature profiles are essentially on top of each other. This is due to the efficient energy exchange in N_2-e^- interactions [53]. For this reason, in what follows, the vibrational and free-electron temperatures are indicated as a unique temperature by means of the notation T_{ve} .

4.1. Assessment of NLTE effects

Before investigating in detail NLTE effects, an LTE simulation is performed and compared with the NLTE results to assess the extent of the departure from equilibrium. The pressure is set to 10000 Pa as, for this relatively high value, LTE conditions are often assumed [17].

Figure 2 compares the LTE and NLTE translational-rotational temperature, Joule heating and electric field distributions. Close to the wall, the curvature of the LTE

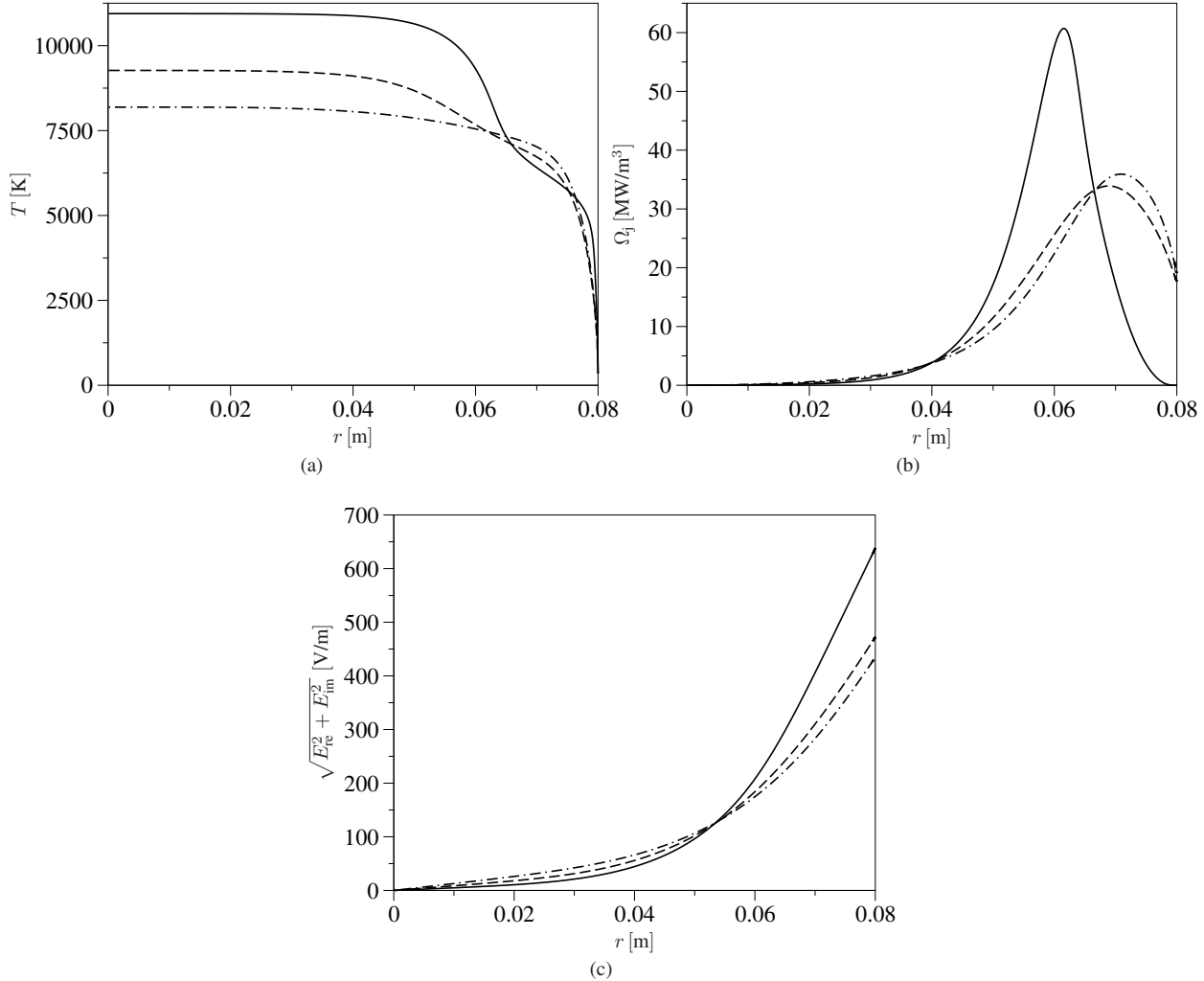


Figure 2: LTE and NLTE translational-rotational temperature (a), Joule heating (b) and induced electric field magnitude (c) distributions at 10 000 Pa (unbroken line LTE, dashed line MT, dotted-dashed line StS).

temperature distribution changes sign. This is a consequence of the non-monotone behavior of the equilibrium total thermal conductivity of the working gas (nitrogen). The same trend is also found in the MT solution (though less enhanced), while the one predicted by the StS model does not exhibit any sign change in its curvature. Both NLTE models predict that the gas is in thermal equilibrium close to the axis (the free-electron temperature is not shown in Figure 2a), though the equilibrium is different between the MT and StS solutions. In both the LTE and NLTE simulations, the temperature is maximum on the axis, due to the absence of radiative losses in the plasma [7, 8]. Overall, the LTE solution predicts higher temperature values, with the difference being maximum on the axis. This is a general trend observed in all the simulations performed in this work (and also in the multi-dimensional results obtained by other investigators in [17, 20]). In NLTE conditions, the temperature is lower because the plasma is heated over a wider region compared to LTE conditions. This is confirmed by the Joule heating distribution shown in Figure 2b. The results in

Figure 2 show that, even when adopting relatively high pressure values, the LTE assumption can lead to a severe overestimation of the gas temperature and, as a related consequence, to a prediction of the chemical composition. It is worth to recall that in the present work, the effects of a macroscopic gas flow (which enhance non-equilibrium) are neglected.

4.2. StS vs MT

After assessing the importance of NLTE effects, the predictions obtained by the StS and MT models are compared in Figure 3 in terms of temperature and N mole fraction. For both the StS and MT solutions, decreasing the pressure has the effect of enhancing thermal non-equilibrium. In the case of the MT model, the translational-rotational temperature is maximum on the axis and decreases monotonically when approaching the wall.

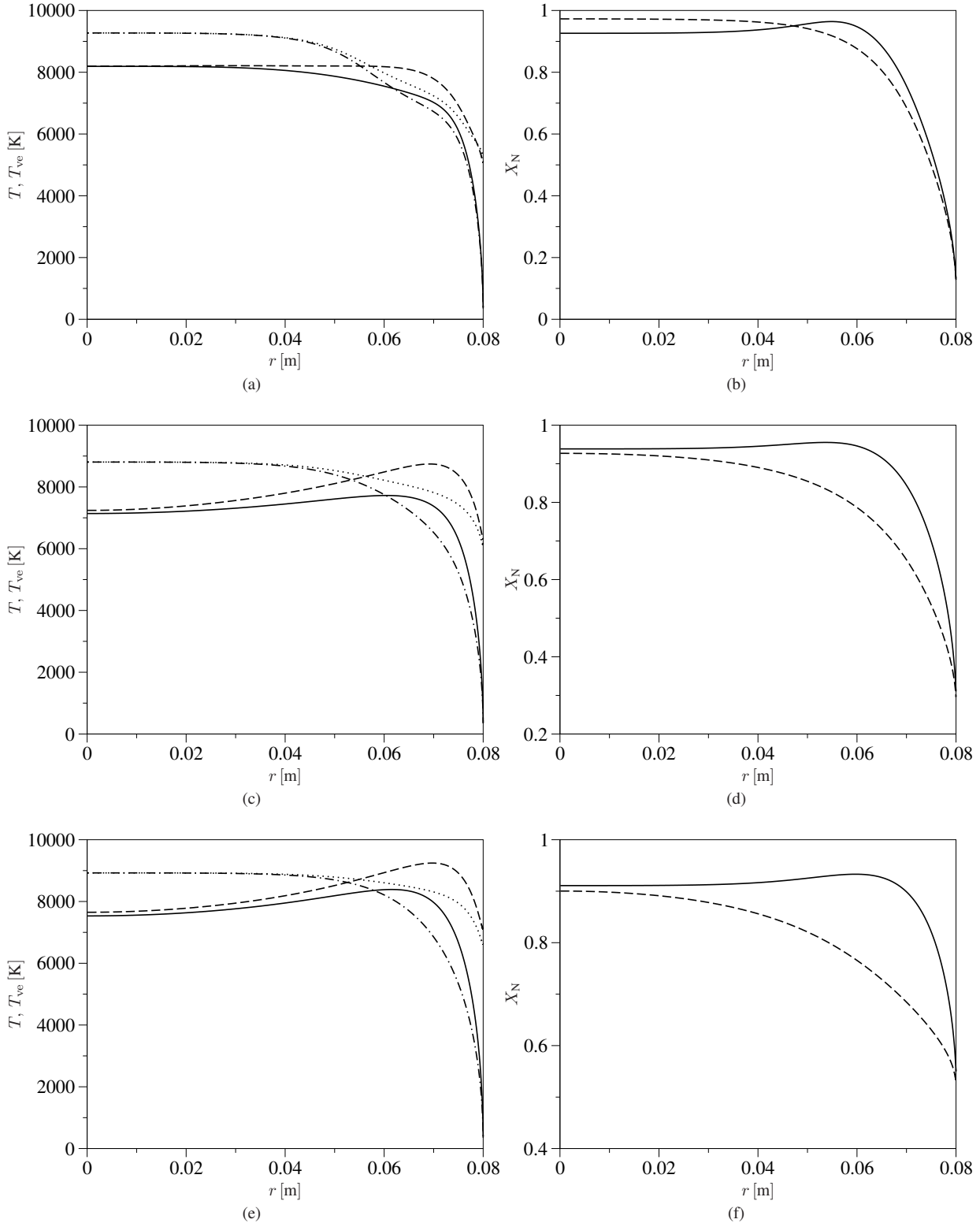


Figure 3: Comparison between the StS and MT solutions in terms of temperature (left) and N mole fraction (right) at different pressures: (a)-(b) $p = 10\,000$ Pa, (c)-(d) $p = 5\,000$ Pa, (e)-(f) $p = 3\,000$ Pa (in (a), (c) and (e) unbroken line T StS, dashed line T_{ve} StS, dotted-dashed line T MT, dotted line T_{ve} MT; in (b), (d) and (f) unbroken line StS, dashed line MT).

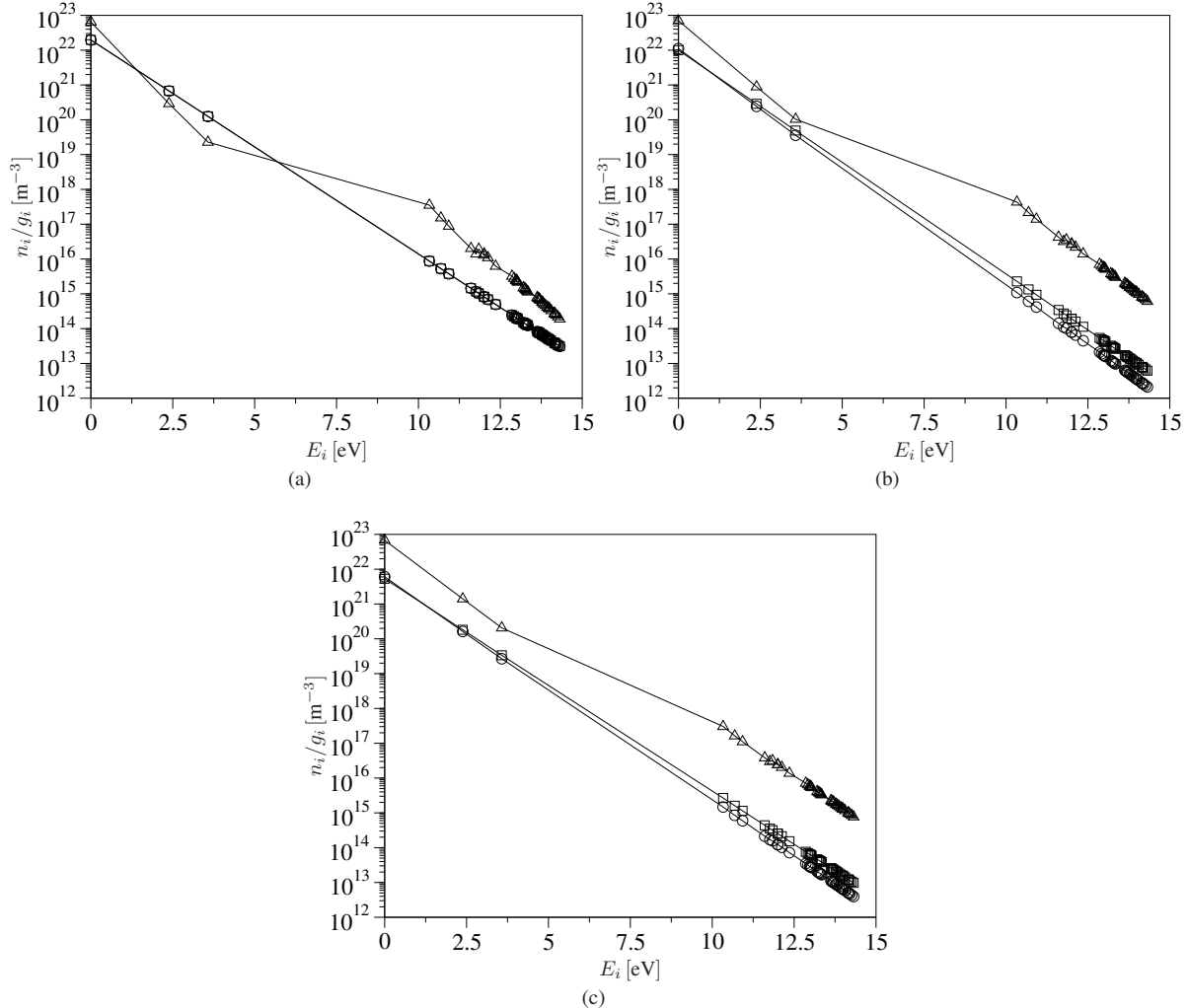


Figure 4: Normalized population of the electronic levels of N at different pressures: (a) $p = 10\,000\text{ Pa}$, (b) $p = 5000\text{ Pa}$, (c) $p = 3000\text{ Pa}$ (line with circles $r = 0\text{ m}$ [axis], line with squares $r = 0.04\text{ m}$, line with triangles $r = 0.08\text{ m}$ [wall]).

On the other hand the free-electron temperature increases, reaches a maximum and then decreases till reaching the value determined from the adiabatic boundary condition. The observed behavior is due to the balance between the Joule heating (which heats up the electron gas) and the energy loss in elastic and inelastic collisions, and chemical reactions. The peak location of the free-electron temperature moves towards the wall when decreasing the pressure. This is a consequence of the Joule heating distribution (not shown in Figure 3) which becomes sharper and clustered to the wall at lower pressures.

It is worth to notice that, in the StS simulation, (i) the translational-rotational temperature no longer exhibits a monotone behavior and (ii) the axis values of both temperatures are systematically lower than those predicted by the MT model. The differences observed between the StS and MT distribution have an effect, as it should be expected, on the chemical composition of the gas (see Figures 3b, 3d and 3f).

Figure 4 shows the normalized population of the electronic levels of N on the torch axis (circles), in the midpoint of the torch (squares) and at the wall (triangles) at different pressures. The population distributions exhibit significant distortions from a Boltzmann shape only close to the wall (where recombination occurs and the Joule heating is close to its maximum value). Deviations from a Boltzmann distributions are more significant when increasing the pressure due to higher recombination (see Figures 3b, 3d and 3f).

5. CONCLUSIONS

A tightly coupled magneto-hydrodynamic solver for the study of the weakly ionized plasmas found in RF discharges has been developed. A hierarchy of thermophysical models have been added to the solver to model the non-equilibrium effects in atomic and molecular plasmas. These include LTE, multi-temperature and the more so-

phisticated State-to-State models. The governing equations for the flow and electromagnetic fields have been written as a system of time-dependent conservation-laws. Steady-state solutions have been obtained by means of an implicit Finite Volume Method.

Results obtained by using a multi-temperature and State-to-State models have shown that the LTE assumption does not hold and that its use can lead to a wrong prediction of the thermo-chemical state of the gas. The analysis of the translational-rotational and free-electron temperature distributions indicated that non-equilibrium plays an important role close to the walls, due to the combined effects of Ohming heating, and chemical composition and temperature gradients. The accurate investigation of the population of excited electronic states has shown that, in view of the absence of a macroscopic gas flow, non-Boltzmann distributions are limited to a narrow region close to the torch wall.

Future work will focus on (i) including the effects of radiation and macroscopic gas flow and (ii) using more sophisticated State-to-State models to better characterize NLTE effects.

ACKNOWLEDGMENTS

Research of A. Munafò was supported by the University of Illinois at Urbana-Champaign Starting Grant. Research of M. Panesi was supported by the AFOSR Summer Faculty Fellowship Program. Research of J.-L. Cambier was sponsored by (ADD HERE). The authors would like to acknowledge Mr. S. Al-Fuhaid at University of Illinois at Urbana-Champaign for the help provided in the early stage of code development.

REFERENCES

- [1] M. I. Boulos. The inductively coupled R.F. (radio frequency) plasma. *Pure & Appl. Chem.*, 9(57):1321–1352, 1985.
- [2] J. Mostaghimi and M. I. Boulos. In *Inductively Coupled Plasma in Analytical Spectrometry*, pages 949–984, 1992.
- [3] T. B. Reed. Induction coupled plasma torch. *J. Appl. Phys.*, 32(5):821–824, 1961.
- [4] M. P. Freeman and J. C. Chase. Energy transfer mechanism and typical operating characteristics of the thermal rf plasma generator. *J. Appl. Phys.*, 39(1):180–190, 1968.
- [5] R. C. Miller and R. J. Ayen. Temperature profiles and energy balances for an inductively coupled plasma torch. *J. Appl. Phys.*, 40(13):5260–5273, 1969.
- [6] D. C. Pridmore-Brown. Numerical study of the inductive electrodeless discharge. *J. Appl. Phys.*, 41(4):3621–3625, 1970.
- [7] H. U. Eckert. Analysis of thermal induction plasmas dominated by radial conduction losses. *J. Appl. Phys.*, 41(4):1520–1528, 1970.
- [8] H. U. Eckert. Analytical treatment of radiation and conduction losses in thermal induction plasmas. *J. Appl. Phys.*, 41(4):1529–1537, 1970.
- [9] H. U. Eckert. Analysis of thermal induction plasmas between coaxial cylinders. *J. Appl. Phys.*, 43(1):46–52, 1972.
- [10] D. R. Keefer, J. A. Sprouse, and F. C. Loper. The electrodeless arc with radial inflow. *IEEE Trans. Plasma Sci.*, 1(4):71–75, 1973.
- [11] H. U. Eckert. Two-dimensional analysis of thermal induction plasmas in finite cylinders. *J. Appl. Phys.*, 48(4):1467–1472, 1977.
- [12] M. I. Boulos. Flow and temperature fields in the fire-ball of an inductively coupled plasma. *IEEE Trans. Plasma Sci.*, 1(4):28–39, 1976.
- [13] R. M. Barnes and S. Nikdel. Temperature and velocity profiles and energy balances for an inductively coupled plasma discharge in nitrogen. *J. Appl. Phys.*, 47(9):3929–3934, 1977.
- [14] J. Mostaghimi, P. Proulx, and M. I. Boulos. Parametric study of the flow and temperature fields in an inductively coupled r.f. plasma torch. *Plasma Chem. Plasma Process.*, 3(4):199–217, 1984.
- [15] X. Chen and E. Pfender. Modeling of RF plasma torch with a metallic tube inserted for reactant injection. *Plasma Chem. Plasma Process.*, 1(11):103–128, 1991.
- [16] D. Vanden Abeele and G. Degrez. Efficient computational model for inductive plasma flows. *AIAA Journal*, 38(2):234–242, 2000.
- [17] D. Vanden Abeele. *An Efficient Computational Model for Inductively Coupled Air Plasma Flows Under Thermal and Chemical Non-Equilibrium*. PhD thesis, Université Libre de Bruxelles, Bruxelles, Belgium, 2000.
- [18] J. Mostaghimi, P. Proulx, and M. I. Boulos. A two-temperature model of the inductively coupled rf plasma. *J. Appl. Phys.*, 61(5):1753–1759, 1987.
- [19] J. Mostaghimi and M. I. Boulos. Effect of frequency on local thermodynamic equilibrium conditions in an inductively coupled argon plasma at atmospheric pressure. *J. Appl. Phys.*, 68(6):2643–2648, 1990.
- [20] W. Zhang, A. Lani, H. B. Chew, and M. Panesi. Modeling of non-equilibrium plasmas in an inductively coupled plasma facility. AIAA Paper 2014–2235, 2014. 45th AIAA Plasmadynamics and Lasers Conference, Atlanta, GA.
- [21] J.-L. Cambier and S. Moreau. Simulation of a molecular plasma in collisional-radiative nonequilibrium. AIAA Paper 1993–3196, 1993. 24th Plasmadynamics and Laser Conference, Orlando, FL.
- [22] M. Capitelli, I. Armenise, D. Bruno, M. Cacciatore, R. Celiberto, G. Colonna, O. De Pascale, P. Diomede, F. Esposito, C. Gorse, K. Hassouni,

A. Laricchiuta, S. Longo, D. Pagano, D. Pietanza, and M. Rutigliano. Non-equilibrium plasma kinetics: a state-to-state approach. *Plasma sources, science and technology*, 2006. 8th European Sectional Conference on Atomic and Molecular Physics of Ionized Gases.

[23] A. Bultel, B. van Ootegem, A. Bourdon, and P. Vervisch. Influence of Ar_2^+ in an argon collisional-radiative model. *Phys. Rev. E*, 65(4):046406, 2002.

[24] Y. Liu, M. Vinokur, M. Panesi, and T. E. Magin. A multi-group maximum entropy model for thermochemical nonequilibrium. AIAA Paper 2010-4332, 2010. 10th AIAA/ASME Joint Thermophysics and Heat Transfer Conference, Chicago, IL.

[25] Y. Liu, M. Panesi, M. Vinokur, and P. Clarke. Microscopic simulation and macroscopic modeling of thermal and chemical non-equilibrium gases. AIAA Paper 2013-3146, 2013. 44th AIAA Thermophysics Conference, San Diego, CA.

[26] A. Bultel, B. G. Chéron, A. Bourdon, O. Motapon, and I. F. Schneider. Collisional-radiative model in air for earth re-entry problems. *Phys. Plasmas*, 13(4):043502, 2006.

[27] M. Panesi, T. E. Magin, A. Bourdon, A. Bultel, and O. Chazot. Fire II flight experiment analysis by means of a collisional-radiative model. *J. Thermophys. Heat Transfer*, 23(2):236–248, 2009.

[28] M. Panesi, T. E. Magin, A. Bourdon, A. Bultel, and O. Chazot. Electronic excitation of atoms and molecules for the FIRE II flight experiment. *J. Thermophys. Heat Transfer*, 25(3):361–374, 2011.

[29] A. Munafò, A. Lani, A. Bultel, and M. Panesi. Modeling of non-equilibrium phenomena in expanding flows by means of a collisional-radiative model. *Phys. Plasmas*, 20(7):073501, 2013.

[30] M. Panesi, R. L. Jaffe, D. W. Schwenke, and T. E. Magin. Rovibrational internal energy transfer and dissociation of $\text{N}(^4\text{S}_u) + \text{N}_2(^1\Sigma_g^+)$ system in hypersonic flows. *J. Chem. Phys*, 138(4):044312, 2013.

[31] A. Munafò, M. Panesi, and T. E. Magin. Boltzmann rovibrational collisional coarse-grained model for internal energy excitation and dissociation in hypersonic flows. *Phys. Rev. E*, 89(2):023001, 2014.

[32] M. Panesi, A. Munafò, T. E. Magin, and R. L. Jaffe. Study of the non-equilibrium shock heated nitrogen flows using a rovibrational state-to-state method. *Phys. Rev. E*, 90:013009, 2014.

[33] H. P. Le, A. P. Karagozian, and J.-L. Cambier. Complexity reduction of collisional-radiative kinetics for atomic plasma. *Phys. Plasmas*, 20(12):123304, 2013.

[34] F. Esposito and M. Capitelli. Quasi-classical molecular dynamic calculations of vibrationally and rotationally state selected dissociation cross sections: $\text{N} + \text{N}_2(v, j) \rightarrow 3\text{N}$. *Chem. Phys. Lett.*, 302(1):49–54, 1999.

[35] F. Esposito, I. Armenise, and M. Capitelli. N – N_2 state-to-state vibrational relaxation and dissociation rate coefficients based on quasi-classical calculations. *Chem. Phys.*, 331(1):1–8, 2006.

[36] D. W. Schwenke. Dissociation cross-sections and rates for nitrogen. In *Non-Equilibrium Gas Dynamics - From Physical Models to Hypersonic Flights*, Lecture Series. von Karman Institute for Fluid Dynamics, 2008.

[37] R. L. Jaffe, D. W. Schwenke, G. Chaban, and W. Huo. Vibrational and rotational excitation and relaxation of nitrogen from accurate theoretical calculations. AIAA Paper 2008-1208, 2008. 46th AIAA Aerospace Sciences Meeting and Exhibit, Reno, NV.

[38] G. Chaban, R. L. Jaffe, D. W. Schwenke, and W. Huo. Dissociation cross-sections and rate coefficients for nitrogen from accurate theoretical calculations. AIAA Paper 2008-1209, 2008. 46th AIAA Aerospace Sciences Meeting and Exhibit, Reno, NV.

[39] R. L. Jaffe, D. W. Schwenke, and G. Chaban. Theoretical analysis of N_2 collisional dissociation and rotation-vibration energy transfer. AIAA Paper 2009-1569, 2009. 47th AIAA Aerospace Sciences Meeting and Exhibit, Orlando, FL.

[40] I. V. Adamovich, S. O. Macheret, J. W. Rich, and C. E. Treanor. Vibrational relaxation and dissociation behind shock waves. Part 1: kinetic rate models. *AIAA J.*, 33(6):1064–1069, 1995.

[41] I. V. Adamovich, S. O. Macheret, J. W. Rich, and C. E. Treanor. Vibrational relaxation and dissociation behind shock waves. Part 2: master equation modeling. *AIAA J.*, 33(6):1070–1075, 1995.

[42] C. Park. Assessment of two-temperature kinetic model for ionizing air. *J. Thermophys. Heat Transfer*, 3(3):233–244, 1989.

[43] C. Park. Review of chemical-kinetic problems of future NASA missions, I: Earth entries. *J. Thermophys. Heat Transfer*, 7(3):385–398, 1993.

[44] C. Park, J. T. Howe, R. L. Jaffe, and G. V. Candler. Review of chemical-kinetic problems of future NASA missions, II: Mars entries. *J. Thermophys. Heat Transfer*, 8(1):9–23, 1994.

[45] C. Park, R. L. Jaffe, and H. Partridge. Chemical-kinetic parameters of hyperbolic earth entry. *J. Thermophys. Heat Transfer*, 15(1):76–90, 2001.

[46] E. Josyula, W. F. Bailey, and S. M. Ruffin. Reactive and nonreactive vibrational energy exchanges in nonequilibrium hypersonic flows. *Phys. Fluids*, 15(10):3223, 2003.

[47] M. Panesi and A. Lani. Collisional radiative coarse-grain model for ionization in air. *Phys. Fluids*, 25(5):057101, 2013.

[48] M. G. Kapper and J.-L. Cambier. Ionizing shocks in argon. Part I: collisional-radiative model and steady-state structure. *J. Appl. Phys.*, 109(11):113308, 2011.

[49] M. G. Kapper and J.-L. Cambier. Ionizing shocks in argon. Part II: transient and multi-dimensional effects. *J. Appl. Phys.*, 109(11):113309, 2011.

[50] A. Munafò, M. G. Kapper, J.-L. Cambier, and T. E. Magin. Investigation of nonequilibrium effects in axisymmetric nozzle and blunt body nitrogen flows by means of a reduced rovibrational collisional model. AIAA Paper 2012-0647, 2012. 50h AIAA Aerospace Sciences Meeting including the New Horizons Forum and Aerospace Exposition, Nashville, TN.

[51] M. Mitchner and C. H. Kruger. *Partially Ionized Gases*. John Wiley & Sons, 1973.

[52] M. Capitelli, C. M. Ferreira, B. F. Gordiets, and A. I. Osipov. *Plasma Kinetics in Atmospheric Gases*. Springer, 2000.

[53] C. Park. *Nonequilibrium Hypersonic Aerothermodynamics*. Wiley, New York, NY, 1990.

[54] L. Pauling and E. B. Wilson Jr. *Introduction to Quantum Mechanics with Applications to Chemistry*. Dover Books on Physics. Dover Publications, Mineola, NY, 1985.

[55] L. V. Gurvich. *Thermodynamic Properties of Individual Substances*. CRC press, 1994.

[56] V. Giovangigli. *Multicomponent Flow Modeling*. Birkhäuser, Berlin, 1999.

[57] E. Nagnibeda and E. Kustova. *Non-Equilibrium Reacting Gas Flows*. Springer, Berlin, 2009.

[58] L. Landau and E. Teller. Theory of sound dispersion. *Phys. Z Sowjetunion*, 10(1):34–43, 1936. in German.

[59] G. V. Candler and R. W. MacCormack. Computation of weakly ionized hypersonic flows in thermochemical nonequilibrium. *J. Thermophys. Heat Transfer*, 5(3):266–273, 1991.

[60] A. Bourdon and P. Vervisch. Three-body recombination rate of atomic nitrogen in low-pressure plasma flows. *Phys. Rev. E*, 52(2):1888–1898, 1996.

[61] J. H. Ferziger and H. G. Kaper. *Mathematical Theory of Transport Processes in Gases*. North-Holland Pub. Co., 1972.

[62] R. S. Devoto. Transport properties of ionized monatomic gases. *Phys. Fluids*, 9(6):1230–1240, 1966.

[63] T. E. Magin and G. Degrez. Transport properties of partially ionized and unmagnetized plasmas. *Phys. Rev. E*, 70(4):046412, 2004.

[64] T. E. Magin and G. Degrez. Transport algorithms for partially ionized and unmagnetized plasmas. *J. Comput. Phys.*, 198(2):424–449, 2004.

[65] V. Giovangigli. Mass conservation and singular multicomponent diffusion algorithms. *IMPACT Comput. Sci. Eng.*, 2(1):73–97, 1990.

[66] C. W. Gear. *Numerical Initial-Value Problems in Ordinary Differential Equations*. Prentice-Hall, Englewood Cliffs, NJ, 1971.

[67] C. Hirsch. *Numerical Computation of Internal and External Flows*. John Wiley & Sons, New York, NY, 1990.

[68] A. Munafò and T. E. Magin. Modeling of stagnation-line nonequilibrium flows by means of quantum based collisional models. *Phys. Fluids*, 26(9):097102, 2014.